LAWRENCE
LIVERMORE
NATIONAL
LABORATORY

LLNL-CONF-703350

# Snowflake Divertor Configuration Effects on Pedestal Stabilityand Edge Localized Modes in NSTX and DIII-D tokamaks.

V. A. Soukhanovskii

September 20, 2016

26th IAEA Fusion Energy Conference
Kyoto, Japan
October 17, 2016 through October 22, 2016

## Disclaimer

# Snowflake Divertor Configuration Effects on Pedestal Stability and Edge Localized Modes in NSTX and DIII-D tokamaks.

V.A. Soukhanovskii[1], S.L. Allen[1], M.E. Fenstermacher[1], C.J. Lasnier[1], M.A. Makowski[1], A.G. McLean[1], W.H. Meyer[1], D.D. Ryutov[1], F. Scotti[1], R. E. Bell[2], A. Diallo[2], S. P. Gerhardt[2], R. Kaita[2], S. Kaye[2], E. Kolemen[2], B. P. LeBlanc[2], R. Maingi[2], J. E. Menard[2], M. Podesta[2], R.J. Groebner[3], A.W. Hyatt[3], A.W. Leonard[3], T.H. Osborne[3] and T.W. Petrie[3]

[1]Lawrence Livermore National Laboratory, 7000 East Ave, Livermore, CA 94550, USA
[2]Princeton Plasma Physics Laboratory, PO Box 451, Princeton, NJ 08543-0451, USA
[3]General Atomics, PO Box 85608, San Diego, CA 92186-5608, USA

*Corresponding Author:* vlad@llnl.gov

**Abstract:**
Snowflake (SF) divertor experiments in NSTX and DIII-D show that the SF divertor can increase edge magnetic shear (i.e., edge current) and modify pressure profiles of the H-mode pedestal enabling pedestal stability manipulation while maintaining good H-mode confinement ($H_{98y2} \sim 1$). In DIII-D, kinetic profiles were weakly affected by the SF configuration, hence the peeling-ballooning stability did not change. In NSTX, H-modes with suppressed ELMs were obtained with lithium conditioning in the standard divertor configuration. The SF divertor destabilized large ELMs via increase in edge current density. A reduction of ELM-induced divertor peak temperature $T_{surf}$ (and heat flux) in the SF divertor (cf. standard divertor) was observed in both NSTX and DIII-D experiments. It was attributed to a combination of increased ELM ion transit time, power splitting between additional SF strike points, increased deposition area, and additional dissipative losses, which were especially large in the radiative SF divertor.

## 1 Introduction

Mitigation of steady-state divertor heat flux and material erosion in present and future tokamaks is envisioned with the radiative divertor technique and optimized divertor magnetic and plate geometries [1, 2]. However, mitigation of large edge localized mode (ELM) heat fluxes is still an unresolved issue. The unmitigated large ELM energy density is projected to be up to 5-14 MJ-m$^2$. This poses a significant risk for the divertor plate and motivates a development of ELM mitigation and control techniques [3].

A snowflake (SF) divertor configuration uses a second-order poloidal field null, or two nearby first order nulls, to make a larger region of low poloidal field $B_p$ in the

divertor [4, 5, 6]. Poloidal magnetic flux surfaces in the region of the exact second-order null form six separatrix branches with an appearance of a snowflake. Based on encouraging results obtained in experiments [6] on the TCV [7, 8, 9], NSTX [10, 11, 12], DIII-D [13, 14, 15, 16] and EAST [17] tokamaks, the SF divertor is viewed as a potential solution for the tokamak divertor power exhaust problem.

The SF divertor experiments in NSTX and DIII-D demonstrated (cf. standard divertor H-mode) inter-ELM heat transport manipulation (heat flux profile broadening), a significant steady-state peak heat flux reduction due to geometry, radiation, and additional strike points, between and during ELMs, while maintaining good pedestal and core confinement. Existing divertor coils were used for steady-state SF configurations in NSTX ($I_p = 0.9 - 1.0$ MA, $P_{NBI} = 3-5$ MW) and DIII-D ($I_p = 1.2$ MA, $P_{NBI} = 3-5$ MW), in an open geometry divertor with the ion $B \times \nabla B$ drift toward the primary X-point (down) (Fig. 1). The possibility of MHD stability and ELM control with the SF configuration was proposed theoretically [18]. This paper presents analyses of pedestal profiles and ELMs in the SF divertor experiments in NSTX and DIII-D tokamaks, aiming to assess the SF divertor utility to control pedestal stability, ELM sizes and ELM divertor peak heat fluxes.

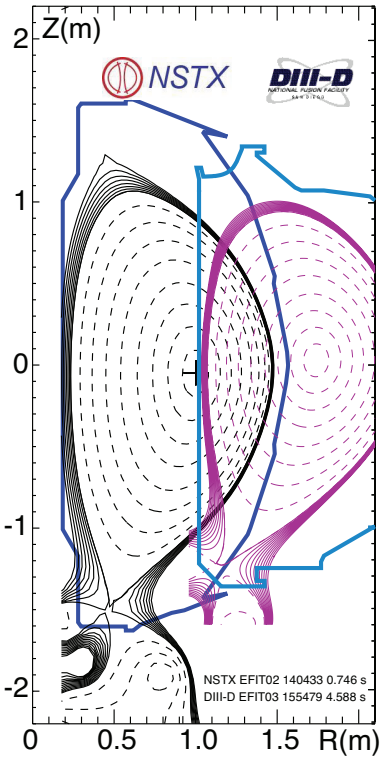


*FIG. 1: Experimental equilibria of the SF divertor configurations in NSTX and DIII-D.*

## 2 Edge profiles and stability

A larger region of very low $B_p$ that extends inside the separatrix in the SF divertor configuration may affect the plasma edge transport, turbulence and MHD stability inside the separatrix, e.g., via increasing magnetic shear $s = \frac{r}{q}\frac{dq}{dr}$ affecting growth rates of certain types of peeling and ballooning modes [18, 19, 20, 21, 22]. ELMs are understood to be due to coupled peeling-ballooning modes, where the ballooning modes are driven by the large edge pressure gradient, and the peeling (kink) modes are driven by the large edge (bootstrap) current produced by the large pressure gradient [23]. In addition, modified radial electric field via enhanced X-point transport, as proposed in Ref. [24], can affect the depth of the $E_r$ well and the shear flow region responsible for the H-mode transition. In this section we summarize pedestal re-

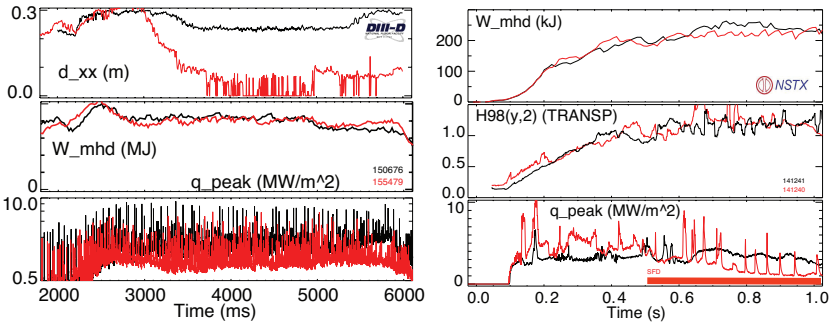


*FIG. 2: Time histories of SF inter-null distance $d_{xx}$, plasma stored energy $W_{MHD}$, and divertor peak heat flux $q_{peak}$ in the standard (black lines) and SF (red lines) configurations in DIII-D (left); $W_{MHD}$, confinement factor H(98,y2) and $q_{peak}$ in NSTX.*

sults from the DIII-D and NSTX SF experiments. Comparisons between the edge SF effects in NSTX and DIII-D are not straightforward: the two tokamaks have a large difference in aspect ratio that makes transport and stability physics different.

The observed SF effects on ELMs are shown in Fig. 2. The core confinement was high (unchanged) with both the standard divertor and the SF divertor configurations, while the ELM regimes differed. In NSTX, lithium conditioning in the amount of 100-200 mg evaporated per discharge was used in the standard divertor H-mode to practically eliminate ELMs. ELM stabilization was achieved by complex changes in pedestal pressure gradient and toroidal edge current density profiles resulting from lithium conditioning [25]. With the SF divertor and lithium conditioning, large ELMs with frequency $f_{ELM}$ =12-35 Hz and $\Delta W_{MHD}/W_{MHD}$ =5-10 % were destabilized. The large SF-induced ELMs led to reduced pedestal carbon concentration (by 30-50 %), suggesting a way of controlling impurity accumulation in lithium-conditioned discharges. In DIII-D, ELMs were weakly affected: $f_{ELM}$ was increased by 5-10 % while the energy lost per ELM $\delta W_{ELM}/W_{ped}$ was reduced by 5-15 % and the peak divertor heat flux and temperatures were also reduced. In both experiments, the increase in edge $q$ values and magnetic shear $s$ were noted. In NSTX they were increased at the very edge in the $\psi_N \geq 0.95$ region, while in DIII-D, both $q_{95}$ and $s_{95}$ showed increase by up to 20-30 % with the SF configuration.

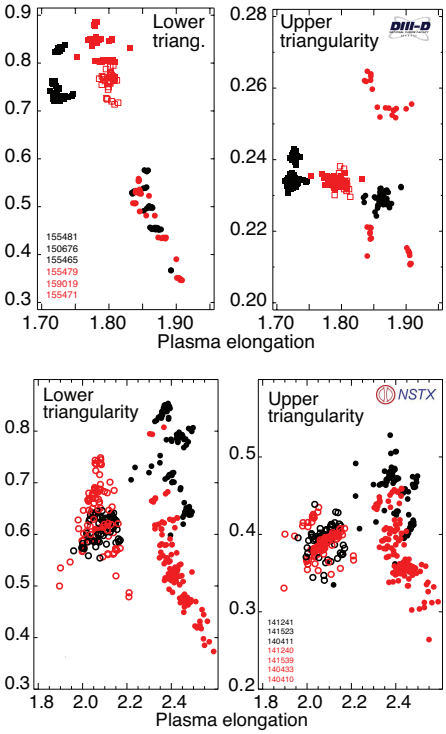


*FIG. 3: Shaping operational space in DIII-D (top) and NSTX (bottom). Lower and upper plasma triangularities vs plasma elongations are shown for the standard (black) and SF divertor (red) configurations.*

**Plasma shaping** Highly shaped plasmas tend to be more stable in both NSTX and DIII-D, with access to smaller-size ELM regimes, higher pedestal pressures and the associated stabilization of certain mode types, e.g., ideal ballooning modes. When a SF divertor configuration is formed, plasma shaping parameters slightly change w.r.t. similar standard divertor discharges because higher divertor coil currents are used, and the position of the lower primary X-point tends to drift inward. The shaping is therefore an external factor that must be considered since the SF discharge stability changes may be partly due to the SF geometry and partly due to the shaping. Shown in Fig. 3 are the elongation ($\kappa$) and upper and lower triangularities $\delta$. In NSTX, two SF scenarios were compared: 1) the SF divertor was formed from a medium-$\delta$ standard divertor configuration; and 2) the SF divertor was formed from a highly triangular plasmas. The medium-$\delta$ SF and standard divertor scenarios were similar in shaping (perhaps, SF were more triangular on the average). In high-$\delta$ scenarios, the primary X-point radial location was similar or more inward in the SF divertor, suggesting higher triangularities. However, lower $\delta$ values were reported due to the presence of the SF secondary X-point. In DIII-D, the high-$\delta$ SF configurations tended to be more elongated and slightly more triangular than the standard divertor ones, whereas

at medium-$\delta$, the shaping parameters were similar. Overall, a 10-15 % enhancement in shaping was observed in NSTX and DIII-D in the SF divertor (cf. standard divertor).

**Edge profiles and gradients** Measured kinetic profiles $(T_e, n_e, T_i, n_C, \Omega)$ were used in a multi-step process to obtain equilibria via a Grad-Shafranov equation edge pressure (including the fast ion pressure) and edge current (including the calculated bootstrap current) constraints. The process is known as "kinetic EFIT" and was done using OMFIT [26]. Edge profiles were used for evaluation of pressure gradient and toroidal current density changes and pedestal stability with the SF divertor. In DIII-D, kinetic profiles were weakly affected by the SF configuration [13, 27]. The pedestal energy remained constant. Edge $dp_{tot}/d\psi_N$ and $J_{tor}(\psi_N)$ were similar in the plasmas with the standard and SF divertor configurations: both the radial location of the peak values and the peaks are similar. This was consistent with the observed weak changes in the ELM regime. Shown in Fig. 4 is the peeling-ballooning stability calculation performed using the ideal MHD stability code ELITE [28, 29] for toroidal modes with $n = 5 - 25$. Both pedestals with the standard and SF divertors similarly appear to be at the stability boundary on the unstable current-limited side, with most unstable modes $n = 10, 15$. The SF divertor-induced increase of magnetic shear in the poloidally localized region resulted in a small (10-15 %) increase in the midplane and did not affect significantly the peeling-ballooning mode structure or stability.

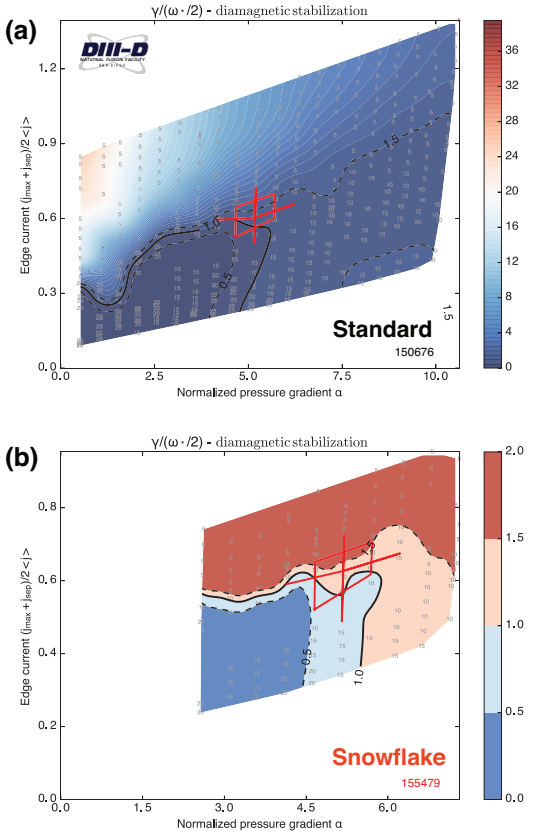


*FIG. 4: Edge stability diagrams (contours of the maximum linear growth rate normalized to stabilization rate) for DIII-D discharges with the standard divertor (a) and SF (b).*

In NSTX, edge profiles were evaluated at several times since the SF configuration was formed and evolved over 500 ms, concomitantly with radiative detachment of the strike point, making it difficult to clearly separate the effect due to the second SF null. The profiles shown in Fig. 5 indicate that the pressure gradient increased during the SF formation (635 ms), however, relaxed in the radiative SF phase (885 ms), while the edge current density peak increased (635 ms) and shifted toward separatrix (885 ms). Previous calculations indicated that the reference standard divertor discharge

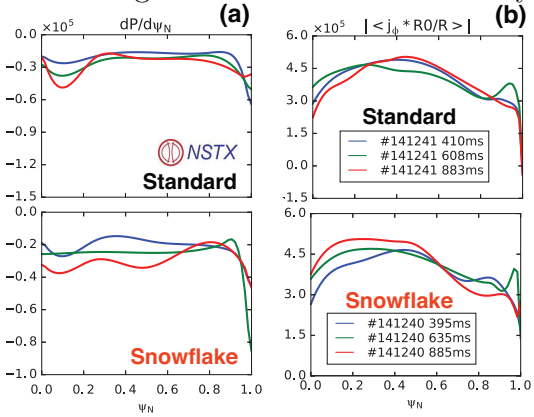


*FIG. 5: Radial profiles of (a) edge total pressure gradient and (b) toroidal current density in NSTX.*

with suppressed ELMs was on the peeling side of the peeling-ballooning stability diagram [25]. The observed changes suggest that with the radiative SF, the pedestal operating point again crossed the peeling boundary and large ELMs were destabilized.

**Pedestal structure** Pressure pedestal height and width $P_{wid}$ reflect pedestal performance and limits. The plasma stored energy is proportional to the pedestal height while $P_{wid}$ scales with pedestal poloidal $\beta_p$. A comparison of pedestal structure parameters (for electron profiles) between the SF divertor and the standard divertor in DIII-D is summarized in Fig. 6. Pedestal heighs and widths were practically unchanged with the SF divertor. The pedestal electron densities were increased by 10-15 % while the electron temperatures were decreased by similar amounts.

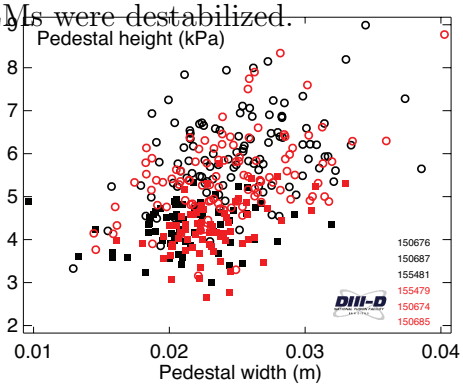


*FIG. 6: Pedestal structure operating space in the DIII-D discharges with standard (black) and SF (red) divertors.*

**Edge radial electric field** The edge electric field determines the velocity shear in the pedestal and, hence, the stability and structure of the H-mode pedestal. Electric potential inside the separatrix in the SF configuration may be affected by the increased prompt ion loss predicted theoretically [24] as the trapped ions spend longer times on the banana trajectories in the null region due to longer field lines, and drift out due to the $B \times \nabla B$ drift. Edge $E_r$ was inferred in both experiments. In DIII-D, $E_r$ was calculated based on kinetic profiles using the NEO code. The radial location of the peak $E_r$ well was unchanged with he SF divertor, while the depth of the $E_r$ well was greater by $\leq 10$ %. In NSTX, $E_r$ was inferred from the radial force balance and measured toroidal and poloidal C III ion temperature and flow velocities just inside the separatrix [30]. In the SF divertor, the inferred $E_r$ values exceed the standard divertor ones by 10-15 %. In the spherical tokamak, higher trapped particle fraction may enhance X-transport in the SF divertor.

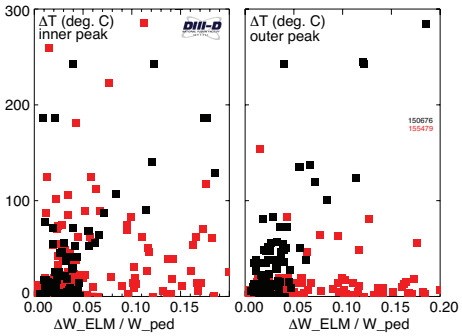


*FIG. 7: Peak ELM divertor surface temperatures in inner and outer divertors as functions of normalized ELM energy loss in DIII-D standard (black) and SF (red) divertors.*

**Edge collisionality and ELM size** The amount of energy lost per ELM, or ELM size, for large Type I ELMs tends to be inversely proportional with pedestal collisionality for the conduction-dominated ELMs, as has been previously observed in DIII-D [3]. The SF configuration increases the field line length inside the separatrix $\pi R q_{95}$ and tends to increase edge collisionality $\nu^*_{ped} = \pi R q_{95}/\lambda_{ee}$ for discharges with otherwise similar pedestal characteristics [15, 16]. Accordingly, energies lost per ELM

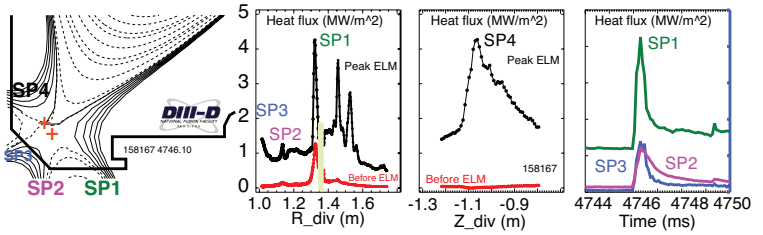


*FIG. 8: Divertor heat flux profiles and peak heat time histories in the attached near-exact SF divertor in DIII-D.*

$\Delta W_{ELM}$ (as well as $\Delta W_{ELM}/W_{ped}$) were lower by 5-15 % in the DIII-D SF discharges (cf. similar standard divertor discharges) for the ELMs with $\Delta W_{ELM}/W_{ped} \leq 0.10$. In NSTX, comparisons of SF-induced ELMs to standard divertor ELMs were not possible due to uncertainties in ELM energies.

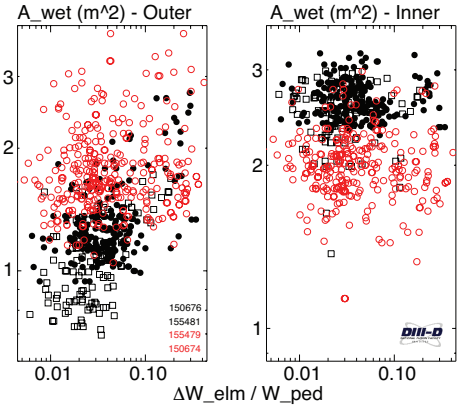


*FIG. 9: Inner and outer divertor ELM wetted area measured in DIII-D standard (black symbols) and SF (red symbols) divertor configurations.*

## 3 Divertor ELM heat fluxes

A reduction of ELM-induced divertor peak surface temperature $T_{surf}$ (and heat flux) in the SF divertor (cf. standard divertor) was noted in both NSTX and DIII-D (Fig. 7) experiments. Tokamak ELM studies have established that a transient (ELM) heat pulse causes a divertor $T_{surf}$ rise $\Delta T_{surf} \sim \Delta W_{div}/(A_{wet}\tau_{ELM})^{1/2}$, where $\Delta W_{div}$ is the total deposited energy, the ELM-wetted area is $A_{wet} = P_{div}/q_{peak}$, and $\tau_{ELM}$ is the energy deposition time [3]. The deposition time is proportional to the pedestal thermal ion transit time to the strike point $\tau_{\|} = L_{mp-sp}/c_{ped}$, where $c_{ped}$ is the ion sound speed. Each of the above quantities can be analyzed in the experiment to provide a semi-quantitative argument of ELM peak temperature and heat flux reduction. We note two caveats in the analysis presented below. First, the present analysis does not provide quantitative assessment of the fractions of $\Delta W_{div}$ that were deposited in the inner and outer divertors. In a number of tokamaks, a larger fraction of $\Delta W_{div}$ is typically deposited in the inner divertor. However, in NSTX, heat fluxes on the inner vertical target were not measured. In the DIII-D standard divertor discharges analyzed in this study, IR thermography indicated that larger or equal fractions of ELM power were deposited in the outer divertor. Second, in a number of DIII-D discharges, heat deposition on the divertor surface extended well outside the divertor SOL, thereby not necessarily affected by the SF-induced magnetic and transport effects in the null region.

**DIII-D** A key SF property predicted by theory [5] is that ELM heat flowing into the null-region is mixed in the high $\beta_p$ region and redistributes over the additional separatrix branches and strike points. Divertor ELM heat deposition was studied under attached and detached conditions. Fig. 7 indicates that with higher $\Delta W_{ELM}/W_{ped}$ (5-20 %), lower $\Delta T_{surf}$ were achieved in the attached SF divertor (cf. standard divertor). Higher energy ELMs lead to higher transient pressure (higher $\beta_p$) in the SF null region. This, according to theory, would lead to stronger convective mixing, and as a result, lower ELM fluxes per separatrix branch (strike point). Fig. 8 shows typical ELM heat deposition in the attached SF divertor. Peak heat fluxes up to 4 MW/m$^2$ are measured in both the inner and outer strike points. Additional strike points (SP2 and SP3) also receive heat, however, the fraction is small, 5-10 %, similar to between ELM heat deposition fractions previously reported [15]. A large fraction of ELM energy is deposited on the divertor shelf outside the outermost trike point SP1. The heat flow into the shelf pattern was unaffected by the SF configuration, except the peaks in the SF configuration are lower. Time histories of $q_{peak}$ demonstrate that the heat flux rise and decay times in the connected strike points

SP1 and SP3 are faster than in the strike point SP2 which is not directly connected, suggesting that some heat diffusion across the null region took place.

We can now examine the factors affecting ELM peak surface temperature and heat fluxes. The time $\tau_{\|}$ is proportional to the experimentally measured peak divertor heat rise time $\tau_{IR}$. The transit time $\tau_{\|}$ is typically longer in the SF geometry due to a greater connection length, the latter also resulting in a temporal dilution of the energy pulse and reducing its peak [31]. The divertor ELM energy density $W_{div}/A_{wet}$ is also reduced, due to a reduction of $\Delta W_{ELM}$ and an increase of the ELM plasma-wetted area. Integration of ELM heat fluxes in the inner and outer divertor shows that outer-inner ELM power ratio is 2-4 in the SF configuration, whereas in the standard divertor, it is 4-8. A comparison of the ELM-wetted areas $A_{wet}$ is shown in Fig. 9. The outer $A_{wet}$ accounted for the strike points SP1, SP2, and SP3 in the SF divertor. It was greater by up to 50 % (cf. the standard divertor). The SF inner divertor $A_{wet}$ was reduced by up to 30 %.

If a greater ELM energy fraction is deposited in the inner divertor than in the outer divertor, the SF-minus configuration with the secondary null in the high-field-side (HFS) SOL can be used to mitigate the divertor ELM impact, as shown in Fig. 10. In this attached SF-minus divertor, ELM heat fluxes were shared over SP4, SP3 and SP2, with lower peak heat fluxes. A significant reduction of the inner divertor peak heat flux was observed, as the heat flux was split magnetically between SP4 and SP2. ELM heat deposition showed a multi-peak pattern outside of the SOL far from the outermost SP1 in both divertor configurations. Peak heat fluxes in the pattern were reduced in the SF divertor. The pattern could be a result of error field induced magnetic manifolds. Additional studies are needed to understand the mechanism of formation and heat transport in these magnetic manifolds outside the SOL.

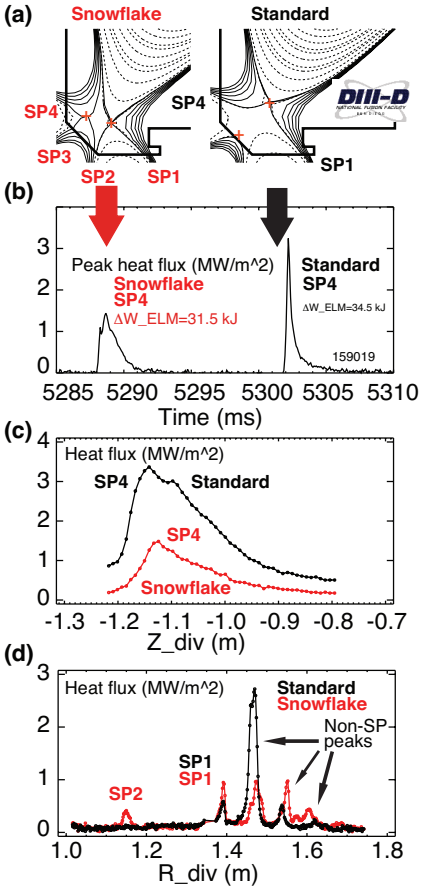


*FIG. 10: Comparison of ELMs in HFS SF-minus and standard attached divertors in DIII-D. (a) Magnetic equilibria; (b) Peak inner divertor heat flux time histories; (c) Inner target and (d) outer target heat flux profiles.*

**NSTX** Comparisons could be made between an attached quasi-SF-minus (forming SF), and a radiative SD-minus with a partial strike point detachment, since the SF-minus configuration evolved over time. Divertor profiles at peak ELM times are compared for the SF and standard geometries in Fig. 11. The ELMs caused $\Delta W_{MHD}$ drops in the range $9-25$ kJ. Heat was transported to the primary and secondary strike points in the SF-minus configuration. Peak heat fluxes at ELM peak times were reduced in the SF configuration (cf. standard divertor). At earlier times, significant radiation increase occurred only in the primary divertor leg in the quasi-SF-minus. At later times, C III and C IV radiation filled the entire divertor volume in the radiative SF divertor(cf. narrow radial SOL region in the standard divertor). Plasma

slab model with coronal impurity radiation calculations indicated that it was possible to dissipate ELM energy of 10-25 kJ through carbon radiation and charge exchange losses via a longer loss length. ELMs did not burn through the SF divertor plasma in NSTX, the SF divertor remained in low-temperature, high density recombining state.

# 4 Summary

The SF divertor can modify pedestal and ELM characteristics via a larger area of low poloidal field in the divertor region and the associated modifications in magnetic geometry properties both inside and outside the separatrix, as demonstrated by the NSTX and DIII-D experiments. The modifications are generally beneficial and can be further developed into ELM control scenarios and ELM mitigation techniques.

**Acknowledgments** This work was performed under the auspices of the U.S. Department of Energy under Contracts DE-AC52-07NA27344, DE-AC02-09CH11466 and DE-FC02-04ER54698. We thank the entire NSTX and DIII-D Teams for technical, engineering and computer support as well as for plasma and diagnostic operations. DIII-D data shown in this paper can be obtained in digital format by following the links at https://fusion.gat.com/global/D3D_DMP.

# References

[1] ITER Physics Expert Group et al., Nucl. Fusion **39** (1999) 2391.
[2] LOARTE, A. et al., Nucl. Fusion **47** (2007) S203.
[3] LEONARD, A. W., Phys. Plasmas **21** (2014).
[4] RYUTOV, D., Phys. Plasmas **14** (2007) 064502.
[5] RYUTOV, D. et al., Plasma Phys. Control. Fusion **54** (2012).
[6] RYUTOV, D. D. et al., Phys. Plasmas **22** (2015).
[7] PIRAS, F. et al., Phys. Rev. Lett. **105** (2010) 155003.
[8] REIMERDES, H. et al., Plasma Phys. Control. Fusion **55** (2013).
[9] VIJVERS, W. et al., Nucl. Fusion **54** (2014) 023009.
[10] SOUKHANOVSKII, V. et al., Nucl. Fusion **51** (2011) 012001.
[11] SOUKHANOVSKII, V. et al., Phys. Plasmas **19** (2012) 082504.
[12] SOUKHANOVSKII, V. et al., J. Nucl. Mater. **438** (2013) S96.
[13] ALLEN, S. L. et al., in *Proc. 24th IAEA FEC, San Diego, 2012*, Paper PD/1-2, Slides available at https://fec2012.iaea.org/.
[14] HILL, D., Nucl. Fusion **53** (2013) 104001.
[15] SOUKHANOVSKII, V. A. et al., in *Proc. 25th IAEA FEC, St. Petersburg, 2014*, Paper EX/7-4.
[16] SOUKHANOVSKII, V. et al., J. Nucl. Mater. **463** (2015) 1191.
[17] CALABRÒ, G. et al., Nucl. Fusion **55** (2015) 083005.
[18] RYUTOV, D. et al., in *Fusion Energy 2008 (Proc. 22nd Int. Conf. Geneva, 2008)*, CD-ROM file IC/P4-8, Vienna:IAEA.
[19] RYUTOV, D. et al., in *Proc. 24th IAEA FEC, San Diego, 2012*, Paper TH/P4-18.
[20] FARMER, W. et al., Phys. Plasmas **20** (2013) 092117.
[21] FARMER, W., Phys. Plasmas **21** (2014) 042114.
[22] MA, J. et al., Nucl. Fusion **54** (2014) 033011.
[23] DOYLE, E. et al., Nucl. Fusion **47** (2007) S18.
[24] RYUTOV, D. et al., Phys. Plasmas **17** (2010) 014501.
[25] MAINGI, R. et al., Phys. Rev. Lett. **103** (2009) 075001.
[26] MENEGHINI, O. et al., Nucl. Fusion **55** (2015) 083008.
[27] YAMADA, H., Nucl. Fusion **53** (2013) 104025.
[28] SNYDER, P. B. et al., Phys. Plasmas **9** (2002) 2037.
[29] WILSON, H. R. et al., Phys. Plasmas **9** (2002) 1277.
[30] BIEWER, T. M. et al., Rev. Sci. Instrum. **75** (2004) 650.
[31] ROGNLIEN, T. et al., J. Nucl. Mater. **438** (2013) S418.

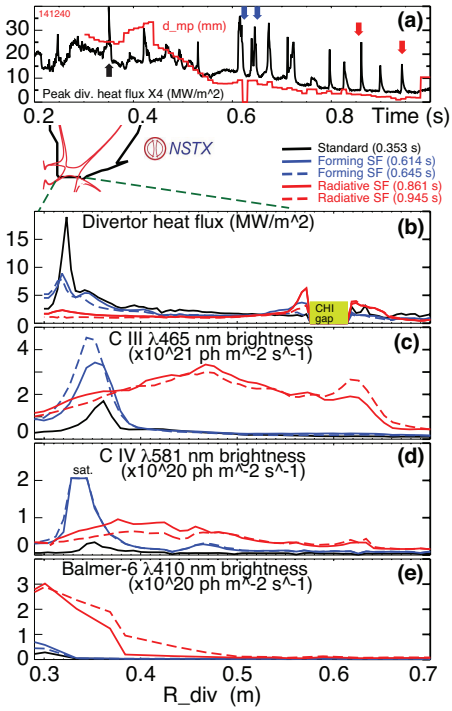


*FIG. 11: (a) Time histories of peak divertor heat flux and inter-null distance projected to the midplane $d_{mp}$ in NSTX SF-minus H-mode discharge; (b)-(e) Divertor profiles in the standard attached, quasi-SF attached, and radiative SF-minus divertors at peak ELM times.*